# Computational Fluid Radiative Dynamics of The Galileo Jupiter Entry at 47.5 km/s

Luís Miguel dos Santos Fernandes
luis.fernandes@ist.utl.pt

Instituto Superior Técnico, Lisboa, Portugal

May 2019

**Abstract**

On December 7th, 1995, the Galileo descent probe entered Jupiter's atmosphere at a relative velocity of 47.4 $\mathrm{km\,s^{-1}}$. Data collected during flight revealed an unforeseen recession profile: while the stagnation region had been significantly oversized, the shoulder almost completely ablated. In an attempt to understand why numerical predictions diverge from the flight data, several sensitivity studies were performed at the 180 km altitude point. The inaccuracy of the Wilke/Blottner/Eucken model at temperatures above 5,000 K was again confirmed. When applied to Galileo's entry, it predicts a narrower shock with higher peak temperatures compared to the Gupta/Yos model. The effects of He and $H_2$ line-by-line radiation were studied. Inclusion of these systems increased the radiative heating by 10% at the stagnation point, even when precursor heating is unaccounted for. Otherwise, the internal excitation of $H_2$ due to absorption of radiation originating from the highly emitting shock layer promotes $H_2$ emission before dissociation occurs at the shock, resulting in 209% higher radiative heat fluxes. This result emphasizes the importance of $H_2$ radiation, not only on the recession experienced by Galileo, but also for future entries in Gas Giants. Accordingly, thermal non-equilibrium resulted in 25% lower radiative heating when compared to an equilibrium solution, contrary to previous investigations that neglected $H_2$. Ablation product absorption was shown to counteract precursor heating of $H_2$, but the ablation layer temperature must be accurately predicted using a material-response code coupled to the flowfield. Finally, the tangent-slab and ray-tracing models agreed to within 13%.

**Keywords:** Hypersonics, Galileo, Non-Equilibrium, Radiation, Aerothermodynamics

## 1. Introduction

On October 18, 1989, the Galileo orbiter was sent aboard the cargo bay of Space Shuttle Atlantis, carrying a descent probe designed to penetrate the Jovian atmosphere with a set of scientific instruments. The probe officially began its descent on December 7, 1995, at a relative velocity of 47.4 $\mathrm{km\,s^{-1}}$, having decelerated from Mach 50 to under Mach 1 in under 30 seconds and experienced peak heating rates exceeding 300 $\mathrm{MW\,m^{-2}}$ [1, 2]. The extreme heating environment sustained by the probe during its descent remains, until today, one of the most severe ever encountered by a planetary entry capsule. Although the mission was a success, post-flight analysis of the data collected by temperature and ablation sensors installed in the descent probe's thermal protection system (TPS), whose geometry is illustrated in Figure 1, revealed how close it came to completelly ablate near the shoulder. Pre-flight simulations have since been confirmed to present large discrepancies with the flight data when it comes to the expected heat-shield recession, spurring a revival of research aimed at understanding its causes.

Accordingly, a set of thorough sensitivity studies regarding the modeling of different phenomena that have been either neglected or poorly modeled in the

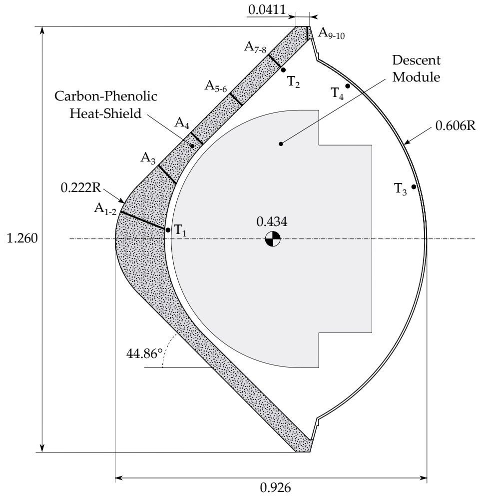

**Figure 1:** Galileo geometry and sensor locations.

past has been conducted. Particularly, the impact of the following physical processes/modeling strategies will be assessed: calculation of transport properties using the Wilke/Blottner/Eucken transport model or the Gupta/Yos model; thermo-chemical non-equilibrium effects; influence of including He and $H_2$ radiation; comparison of tangent-slab and ray-tracing approaches for the computation of radiative heat transfer. This is accomplished by first solving for the flowfield using the SPARK CFD solver, after which the radiative field is computed using the SPARK Line-by-Line (SPARK LbL) radiative code in a decoupled fashion.

In the process, the capabilities of both codes have been enhanced. First, the numerical module responsible for computing the transport properties of the gas in SPARK has been re-structured, now allowing simulation of all Solar System planets' atmospheres using the detailed Gupta/Yos transport model, a feature previously only available for air. Furthermore, the radiative transfer module in SPARK LbL has been rebuilt from scratch using Fortran Object-Oriented programming techniques, improving efficiency of both tangent-slab and ray-tracing routines. This upgrade to both codes was found necessary in order to perform the desired sensitivity studies, while also providing an extension to the capabilities of both numerical libraries.

Sec. 2 presents an overview of past works performed on Galileo's entry in Jupiter. The main difficulties experienced in reproducing the flight data are examined, and the modeling assumptions used in past works are discussed and appraised. Then, the models used in the present work that bring closure to the Navier-Stokes equations are detailed (thermodynamics, chemical-kinetics and transport), and the Wilke/Blottner/Eucken and Gupta/Yos models for transport are compared in Sec. 3. In Sec. 4, the radiative database developed is presented, together with the radiative transfer models implemented. Finally, the results obtained for the 180 km altitude point in Galileo's trajectory are discussed in Sec. 5, and final thoughts are drawn (Sec. 6).

## 2. Literature Review

The Galileo entry has been subject to several studies, not only in the mission preparation phase, for providing a suitable design for the TPS, but also after the flight, since many authors have tried to numerically replicate the descent probe's heat shield recession. In this section a brief timeline of these predictions is given.

### 2.1. Mission Preparation and Flight Data Treatment

Two sets of ground-based experiments conducted independently have previously studied the chemical kinetics of $H_2-He$ mixtures. In 1972, Leibowitz performed electric arc driven shock tube experiments on such mixtures, having explored shock velocities ranging from 13 to 20 $\mathrm{km\,s^{-1}}$ [3]. Similar experiments were conducted by Livingston and Poon in 1976 for shock velocities between 26 and 46 $\mathrm{km\,s^{-1}}$ [4]. Both studies assessed the ionization relaxation processes between atomic hydrogen and electrons in the high-temperature shock layer downstream of the shock wave, and recommended expressions for the chemical kinetic rates in egreement with the experimental measurements were provided[5]. These old experiments are still used today for the validation of theoretical models, emphasizing the value attributed to experimental ground testing.

The data collected in these experiments allowed several pre-flight numerical predictions to be obtained. Moss and Simmonds performed extensive simulations during the mission preparation phase [6]. These ranged from Viscous Shock-Layer (VSL) to Navier-Stokes solutions, studying the effects of distinct physico-chemical processes taking place, such as turbulence, ablation, spallation and wall reflectivity, all under the assumption of chemical equilibrium. Tiwari and Szema also studied the role of thermo-chemical non-equilibrium and precursor heating in Galileo's entry [7], having found a significant increase in both convective and radiative heating compared to an equilibrium solution. The influence of precursor heating is enhanced due to non-equilibrium conditions, and radiative heat fluxes at the stagnation point (SP) were found to increase by 10% when this phenomenon was modeled.

After the mission's success, the flight data regarding the heat shield ablation and temperature captured by the sensors during descent was analyzed by Milos *et al.* [2]. The actual heat shield recession along the wall of the descent probe is shown in Figure 2, and a comparison is provided on the numerical recession obtained by other authors. Moss and Simmonds' pre-flight predictions highlight the classical trend observed for the Galileo mission: the nose recession is largely overpredicted, while the opposite is true in the frustum region. This trend translates the heat fluxes experienced by the probe's surface, which lead to ablation, spallation and sublimation of the probe's TPS.

### 2.2. Numerical Reproduction of Flight Data

Among the first to have studied the problem after the mission, Matsuyama *et al.* performed coupled radiative transfer simulations assuming thermo-chemical equilibrium [8], while assessing the influence of a tangent-slab approximation against an accurate ray-tracing approach for radiative transfer calculations. The ray-tracing approach was found to predict a 10% lower SP radiative heating when compared to the tangent-slab approach.

In 2005, the same authors studied the effects of turbulence coupled with ablation-product injection near the wall [9], having found that turbulent-induced diffusion of ablation products in the shoulder decreased radiation absorption by these carbonaceous species (C, $C_2$ and $C_3$ mostly), allowing for a better prediction of the recession in this region, as their results show in Figure 2.

Subsequently, Furudate *et al.* studied the effects of thermo-chemical non-equilibrium [10], whose effects were shown to reduce the predicted radiative heat fluxes in the SP by as much as 10%, leading to a better agreement in the predicted surface recession over this region. Park also studied the SP radiative heating under chemical equilibrium [11]. The author reported good agreement with the flight data on the SP recession (see Figure 2), provided the effects of spallation and inclusion of vacuum ultraviolet (VUV) bands for $C_2$ and $C_3$ species were incorporated in the radiative analysis. More recently, Reynier *et al.* compiled the state-of-the-art in the modeling of giant-planet atmospheres for convective heating predictions, and reviewed previous attempts in simulating the Galileo entry [1]. The increasing level of detail provided by the improved databases, which are supported by state-to-state kinetic studies, is shown to decrease the convective component of the heat fluxes by between 70% and 85% when compared to older estimates.

It should be noted that all previous studies taking into account the radiation field only considered radiative mechanisms from H, while the effect of He lines and $H_2$ bands, for example, remains unaccounted for. Moreover, the three-dimensional character of radiative transport is rarely included, and modeling of transport properties has, until now, relied on Wilke's mixing rules, despite their poor accuracy at high temperatures. Also, thermo-chemical equilibrium has been assumed in the main studies performed in the past. A thorough study of these effects is still lacking in order to understand the unresolved mysteries regarding the Galileo entry, which is the aim of the present work.

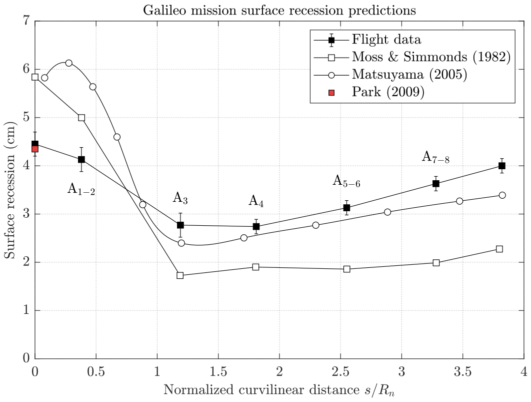

**Figure 2:** Predicted heat shield recession [2, 6, 9].

## 3. Flowfield Modeling

This section provides details on the models used in this work to compute the flowfield properties. These are implemented in the SPARK code, a multi-physics CFD code designed to handle hypersonic flows with high-temperature effects. The thermodynamic and kinetic properties of the flow are described, and a comparison between different models to compute transport properties is presented.

In the present work, the compressible Navier-Stokes equations are used to obtain the macroscopic properties of the flow around the descent probe. These conservation equations are written as

$$\frac{\partial\left(\rho c_s\right)}{\partial t}+\boldsymbol{\nabla}\cdot\left(\rho c_s\boldsymbol{V}\right)=\boldsymbol{\nabla}\cdot\boldsymbol{J_s}+\dot{w}_s \tag{1a}$$

$$\frac{\partial\left(\rho\boldsymbol{V}\right)}{\partial t}+\boldsymbol{\nabla}\cdot\left(\rho\boldsymbol{V}\otimes\boldsymbol{V}\right)=\boldsymbol{\nabla}\cdot[\boldsymbol{\tau}]-\boldsymbol{\nabla}p \tag{1b}$$

$$\frac{\partial\left(\rho e\right)}{\partial t}+\boldsymbol{\nabla}\cdot\left(\rho\boldsymbol{V}e\right)=\boldsymbol{\nabla}\cdot\Big(\boldsymbol{V}\cdot[\boldsymbol{\tau}]-p\boldsymbol{V}-\boldsymbol{q}\Big)\ , \tag{1c}$$

where the heat-flux vector is defined without the radiative source term as

$$\boldsymbol{q}=-\sum_k k_k\boldsymbol{\nabla}T_k+\sum_s\boldsymbol{J_s}h_s\ . \tag{1d}$$

Additionally, the two-temperature model employed in the present work to account for thermal non-equilibrium requires an additional energy conservation equation for the vibrational temperature of $H_2$, described through

$$\frac{\partial\left(\rho e_{\mathrm{v,H_2}}\right)}{\partial t}+\boldsymbol{\nabla}\cdot\left(\rho\boldsymbol{V}h_{\mathrm{v,H_2}}\right)= \\ \boldsymbol{\nabla}\cdot\left(-k_{\mathrm{v,H_2}}\boldsymbol{\nabla}T_{\mathrm{v,H_2}}+\boldsymbol{J}_{\mathrm{H_2}}h_{\mathrm{v,H_2}}\right)+\dot{\Omega}_{\mathrm{V-T}}\ . \tag{1e}$$

### 3.1. Thermodynamics

A seven species mixture composed of H, He, $H_2$, $H^+$, $He^+$, $H_2{}^+$ and $e^-$ was assumed in the present work, similar to the one employed by Reynier *et al.* and used in several other post-flight studies [1, 10, 12, 9]. Jupiter's unperturbed atmosphere is assumed to consist of 86.4% $H_2$ and 13.6% He, in mole percent, the value measured during the actual flight as reported by Milos *et al.* [2]. The thermodynamic properties of the gas are computed from the classical high-temperature results of statistical thermodynamics.

### 3.2. Chemical Non-Equilibrium

Chemical non-equilibrium is taken into account by solving a mass conservation equation for each species separately (Eq. (1a)). The mass source term is modeled via the usual relation expressing the net rate

**Table 1:** Kinetic model employed in the present work.

| Reaction | Process |
|---|---|
| R1 | $\mathrm{H_2} + \mathrm{H} \longleftrightarrow \mathrm{H} + \mathrm{H} + \mathrm{H}$ |
| R2 | $\mathrm{H_2} + \mathrm{He} \longleftrightarrow \mathrm{H} + \mathrm{H} + \mathrm{He}$ |
| R3 | $\mathrm{H_2} + \mathrm{H_2} \longleftrightarrow \mathrm{H} + \mathrm{H} + \mathrm{H_2}$ |
| R4 | $\mathrm{H_2} + \mathrm{H^+} \longleftrightarrow \mathrm{H} + \mathrm{H} + \mathrm{H^+}$ |
| R5 | $\mathrm{H_2} + \mathrm{e^-} \longleftrightarrow \mathrm{H} + \mathrm{H} + \mathrm{e^-}$ |
| R6 | $\mathrm{H} + \mathrm{e^-} \longleftrightarrow \mathrm{H^+} + 2\,\mathrm{e^-}$ |
| R7 | $\mathrm{H} + \mathrm{H} \longleftrightarrow \mathrm{H^+} + \mathrm{e^-} + \mathrm{H}$ |
| R8 | $\mathrm{H} + \mathrm{He} \longleftrightarrow \mathrm{H^+} + \mathrm{e^-} + \mathrm{He}$ |
| R9 | $\mathrm{He} + \mathrm{e^-} \longleftrightarrow \mathrm{He^+} + 2\,\mathrm{e^-}$ |
| R10 | $\mathrm{H_2}^+ + \mathrm{e^-} \longleftrightarrow \mathrm{H} + \mathrm{H}$ |

resulting from the forward and backward reactions:

$$\frac{\dot{w}_s}{\mathscr{M}_s} = \sum_r \Delta\nu_{sr} \left\{ k_{f,r} \prod_s [\mathrm{X}_s]^{\nu'_{sr}} - k_{b,r} \prod_s [\mathrm{X}_s]^{\nu''_{sr}} \right\} , \tag{2}$$

where the forward reaction rates $k_{f,r}$ are computed from the usual Arrhenius equation and $k_{b,r}$ is obtained from the equilibrium constant. Several kinetic schemes regarding entry into Gas Giant atmospheres can be found throughout the literature [7, 1, 10, 3], all of which highlight the importance of properly modeling $\mathrm{H_2}$ dissociation. The kinetic model employed in the present work is presented in Table 1, and the Arrhenius rates employed are those obtained experimentally by Leibowitz and Kuo [3], complemented with the associative ionization reaction rate for $\mathrm{H_2}^+$ used by Furudate [10].

### 3.3. Thermal Non-Equilibrium

Thermal non-equilibrium was studied using a two-temperature model that allows for the vibrational energy levels of $\mathrm{H_2}$ to be populated according to a Boltzmann distribution at a temperature $T_{\mathrm{v,H_2}}$ different from the remaining thermal modes, which are assumed thermalized at $T_{\mathrm{tr}}$. In the radiative analysis, both $T_{\mathrm{e^-}}$ and $T_{\mathrm{v,H_2}}$ are assumed in equilibrium, as vibrational-electronic energy exchange is very efficient. The energy source term $\dot{\Omega}_{\mathrm{V-T}}$ present in Eq. (1e) is modeled using the traditional Landau-Teller equation. Vibrational relaxation times are obtained from Millikan-White's correlation, with coefficients provided by Palmer *et al.* [13].

### 3.4. Transport

One important outcome of this work was the implementation of an updated database along with an improved Gupta/Yos formulation in SPARK, allowing this transport model to be applied to atmospheres other than Earth's. Viscosity, thermal conductivity and mass diffusion are typically computed using the Wilke/Blottner/Eucken model (abbreviated to Wilke from now on), which is known to provide inaccurate results as temperatures increase beyond the onset of ionization. Details for both transport models are provided in the main text. The more detailed Gupta/Yos model, taking into account the effect of non-diagonal terms in the Chapman-Enskog formulation, was also considered (*Gupta/Yos 2nd Order*). Both transport models were compared, and verification was performed against literature data. The results for viscosity and thermal conductivity are presented in Figure 3. The main takeaway from this comparison is the inadequacy of the Wilke transport model above 5,000 K. Additionally, the two Gupta/Yos models implemented also present significant differences, showing the typically neglected impact of the non-diagonal terms in the Gupta/Yos formulation. Thus, the *2nd Order* model was retained for subsequent simulations using the Gupta/ Yos theory.

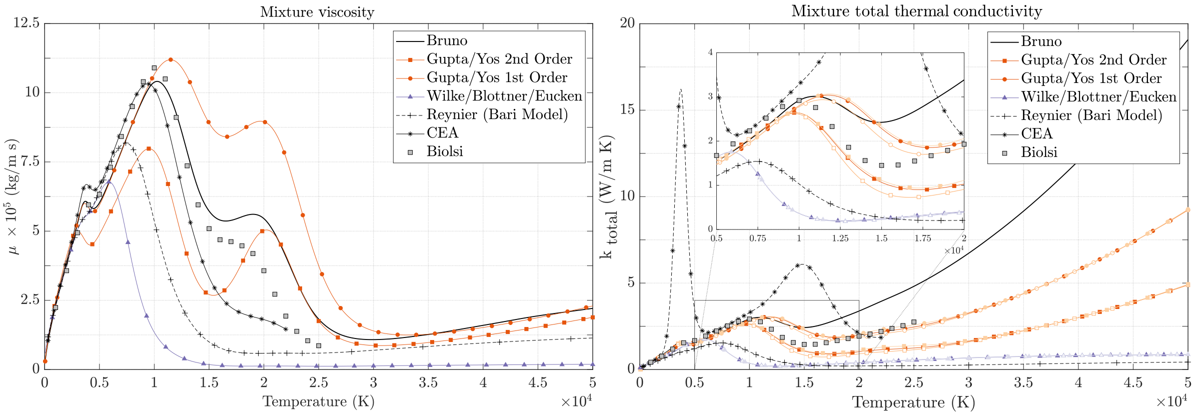

**Figure 3:** Comparison of transport properties obtained from various models and literature data for equilibrium $\mathrm{H_2}-\mathrm{He}$ mixture at 1 atm. The different shades of the same color on the right correspond to using different thermodynamic models: dark filled markers - Analytic model; light filled markers - Capitelli coefficients; light open markers - NASA9 coefficients.

## 4. Radiation Modeling

The definition of a spectral database suited to the Galileo entry conditions has been carried out. The atomic spectral database accounts for as much radiative transitions as possible using the data available in NIST [14], and a general semiempirical function was developed for the Stark broadening mechanisms of hydrogenoïd species. Molecular $H_2$ transitions are also considered, in an effort to determine its impact using a line-by-line approach. Finally, these discrete atomic and diatomic transitions have been complemented by a data set for continuum transitions (bound-free photo-dissociation/ photo-ionization, and free-free bremmstrahlung). A detailed description of the spectral database is available in the dissertation.

### 4.1. Radiation Database Verification

The absorption coefficients obtained with SPARK LbL's spectral database were compared with those published by Perrin *et al.* [15] using the HTGR database. The comparison is performed using an equilibrium $H_2-He$ mixture at 1 atm and initial molar composition in the ratio $H_2 : He = 89 : 11\%$. The spectral absorption coefficients resulting from both databases are presented in Figure 4 for two temperatures: 5,000 K, representative of the boundary layer temperature surrounding Galileo's TPS, and 20,000 K, close to the temperatures found in the high-temperature shock layer.

The results show good agreement between the two spectral databases, although a more pronounced Stark Broadening of H lines is observed in the HTGR database, especially at 20,000 K. As temperatures increase, the molecular absorption lines of $H_2$ present in the UV region are progressively overcome by atomic H Lyman absorption. At lower temperatures, as in the 5,000 K case presented, these molecular absorption mechanisms are still quite important. This raises the question of whether or not the assumption of neglecting $H_2$ radiative processes is reasonable, as has been almost exclusively done in the past. There are two regions in the flow where $H_2$ exists in significant amounts: near the wall, where atomic H recombination occurs, and at the shock location, just before the temperatures increase beyond the onset of dissociation. The increased emission from $H_2$ transitions in the shock region, together with the potential increase in absorption resulting from inclusion of these mechanisms in the boundary layer, were investigated in the present work.

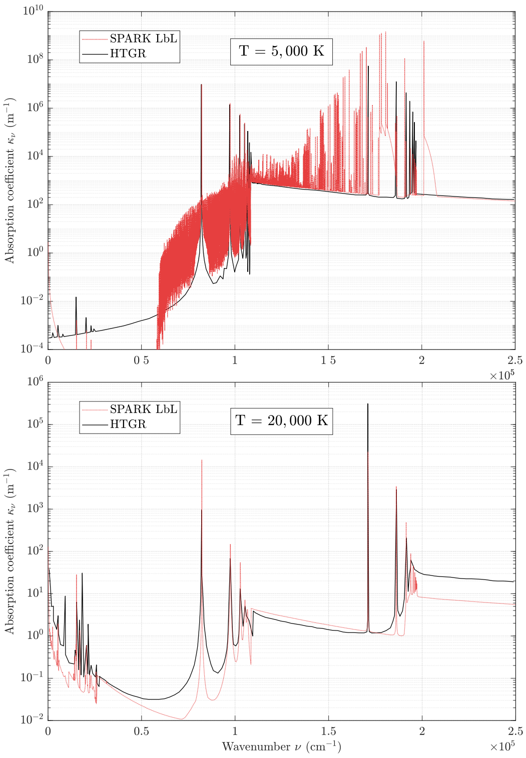

**Figure 4:** SPARK LbL and HTGR's databases compared at 5,000 K (top) and 20,000 K (bottom).

### 4.2. Radiative Transfer Models

The energy transfer processes resulting from radiative transitions occurring everywhere in the flowfield is modeled through the solution of the radiative transfer equation, which may be written in the form

$$I_\nu^{\theta,\phi}(L) = I_{\nu,0}^{\theta,\phi} e^{-\tau_\nu(L)} + \int_0^{\tau_\nu(L)} \frac{j_\nu}{\kappa_\nu} e^{-(\tau_\nu(L)-\tau_\nu)} \, \mathrm{d}\tau_\nu \ , \tag{3}$$

expressing the spectral intensity of radiation as a function of the spectral coefficients and optical thickness at a position $L$ along the line of sight specified by the direction $(\theta, \phi)$. The optical thickness is defined as the integral of the absorption coefficient over a given distance, that is

$$\tau_\nu\,(s) = \int_0^s \kappa_\nu \ \mathrm{d}s' \ . \tag{4}$$

The radiative heating the probe experiences during entry is obtained by integrating $I_\nu^{\theta,\phi}$ over the spectral and hemispherical domain, after solving Eq. (3) for the spectral directional intensity at every location along the wall, that is,

$$q_{\mathrm{rad}} = \int_0^\infty \int_0^{2\pi} \int_0^{\pi/2} I_{\nu,\mathrm{wall}}^{\theta,\phi} \cos\theta \sin\theta \ \mathrm{d}\theta \ \mathrm{d}\phi \ \mathrm{d}\nu \ . \tag{5}$$

The formulation often employed to solve Eq. (3) is the tangent-slab approximation, which is known to overpredict the radiative heating at the stagnation region by 10 to 15%, whereas differences of up to 70% have been reported for the shoulder and afterbody regions when compared to the ray-tracing approach.

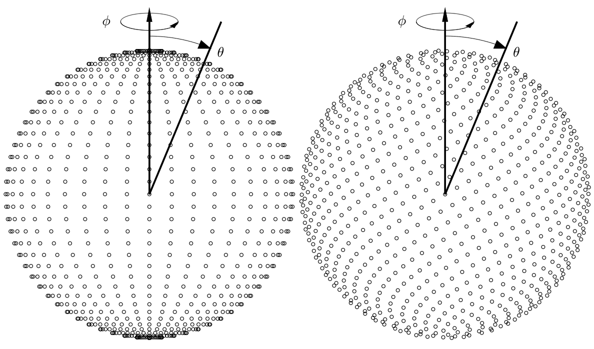

**(a)** Constant $(\Delta\theta, \Delta\phi)$. **(b)** Fibonacci Lattice.

**Figure 5:** Ray distribution strategies compared.

Both models were implemented in a Fortran module and integrated with the SPARK LbL spectral database in an uncoupled approach.

The fundamental assumption behind the tangent-slab approximation is that the flow properties are considered to vary only in the direction normal to the body for the purpose of radiative transfer computations. This approximation prevents radiative transitions to have an impact other than at the wall location directly normal to them, leading to a localized modeling of inherently non-local phenomena. This assumption allows the evaluation of the directional integral in Eq. (3) to be performed analytically, resulting in

$$q_{\text{rad}}^{\text{TS}} = 2\pi \int_0^\infty \int_0^{z_\infty} j_\nu \; \mathscr{E}_2 \left[\tau_\nu (z)\right] \; \mathrm{d}z \; \mathrm{d}\nu \; , \tag{6}$$

where $\mathscr{E}_2(x)$ is the 2nd order exponential integral.

The ray-tracing approach is a more physically consistent method, since it relies on the direct integration of Eq. (3) along a set of rays/directions. The equation is solved for every frequency by marching along a given ray between the upstream and wall boundaries to obtain the spectral intensity $I_{\nu,\text{wall}}^{\theta,\phi}$ at the vehicle's surface, and the radiative heating is then obtained from Eq. (5).

At the heart of the ray-tracing approach is the directional discretization of the hemispherical domain, providing the directions $(\theta, \phi)$ along which Eq. (3) is solved. A simple approach that is often (inadequately) implemented is to select a set of constant $\Delta\theta$ and $\Delta\phi$ values and subdivide the domain into equally spaced intervals, resulting in a cluster of rays at the poles. The alternative technique implemented in the present work relies on the so-called Fibonacci Lattice [16], providing a significant improvement in uniformity when compared to the constant $(\Delta\theta, \Delta\phi)$ grid, as may be observed in Figure 5.

Once the directional discretization is set up and the trajectories of the rays through the flowfield are known, the emission and absorption coefficients are computed along each line of sight by providing the flowfield temperatures and species' number densities to the line-by-line routine. Since the rays don't necessarily pass through the cell's center, where its properties are defined, an approximation must be employed at this stage. The simplest option is to consider the emission and absorption coefficients to be constant along a given cell, inheriting the spectral values of the cell-center. However, this may potentially introduce large spatial integration errors in locations where the mesh is coarse, or if the integration is carried over lengthy rays, in which case the error accumulates with each cell. Another option is to assume that the spectral coefficients vary linearly between cells. This alternative was implemented in SPARK LbL, following the approach developed by Johnston *et al.* [17] for the LAURA/HARA suite of codes at NASA. The three radiative transfer formulations were implemented and compared in the context of the Galileo entry.

The final step in obtaining the surface radiative heating $q_{\text{rad}}$ is the directional integration over the hemisphere, as defined by Eq. (5), followed by an integration over the spectral domain. Regarding the former, a typical integration quadrature cannot be employed since the directional grid constructed from the Fibonacci Lattice is irregular in $\theta$ and $\phi$. This complication may be avoided by using a Monte-Carlo-based integration technique, which is justified by the small number of variables and the large number of rays (samples). The spectral radiative heating at a given wall location is then simply

$$q_\nu = 2\pi \frac{1}{N_{\text{rays}}} \sum_{r=1}^{N_{\text{rays}}} I_{\nu,r} \cos\theta_r \; , \tag{7}$$

where $N_{\text{rays}}$ represents the total number of rays considered for that wall point, and $\theta_r$ is the angle between the ray and the wall normal. The resulting $q_\nu$ is then integrated in frequency using a trapezoidal rule to yield the surface radiative heating.

## 5. Results and Discussion

The simulations performed in the present work focus on the trajectory point at 180 km altitude, where strong non-equilibrium is expected. Table 2 presents the flowfield test matrix simulated in the present work. Reynier *et al.* [1] also studied this point, allowing for qualitative comparisons to be drawn. The

**Table 2:** Test matrix used in the present work [1, 2].

| Case | Alt. (km) | Time (s) | $V$ (m/s) | $T$ (K) | $p$ (Pa) |
|---|---|---|---|---|---|
| Wilke 1T<br>Wilke 2T<br>Gupta/Yos 1T<br>Gupta/Yos 2T | 180 | 42.06 | 46,674 | 161.9 | 27.5 |

influence of the two considered transport models is assessed in both thermal equilibrium and non-equilibrium conditions (1T and 2T), by solving the Navier-Stokes equations assuming laminar flow and an axisymmetric flowfield. All simulations assume an isothermal, non-catalytic wall at 3,000 K. The thermodynamic, kinetic and energy-exchange models described previously were applied, and whenever thermal non-equilibrium was considered, Park's rate-controlling temperature model is applied to the dissociation reactions of $H_2$.

The computational domain surrounding the Galileo probe is illustrated in Figure 6, along with two ARAD sensor locations, representative of mid-body and near-shoulder regions. A structured 72 × 60 mesh was found to properly capture all flowfield features of interest, following a mesh convergence study. The mesh was refined at strong-gradient regions and extended beyond the strong expansion issuing from the shoulder, a feature that was deemed necessary so as to obtain accurate ray-tracing predictions in this region. However, this introduced significant challenges to the simulation of the flow, as the large expansion would reduce the pressure to near-vacuum values, and the solution would easily become unstable. The extreme velocity and small CFL numbers required to stabilize the numerical scheme ( between $10^{-4}$ to $10^{-2}$ at the start, raised to $10^{-1}$ closer to convergence), also meant that very small time steps were used ($\mathcal{O}(10^{-12}$ s)), and convergence took a long time. Furthermore, the upstream velocity had to be incrementally increased until the actual flight velocity was reached, even though an implicit scheme was used.

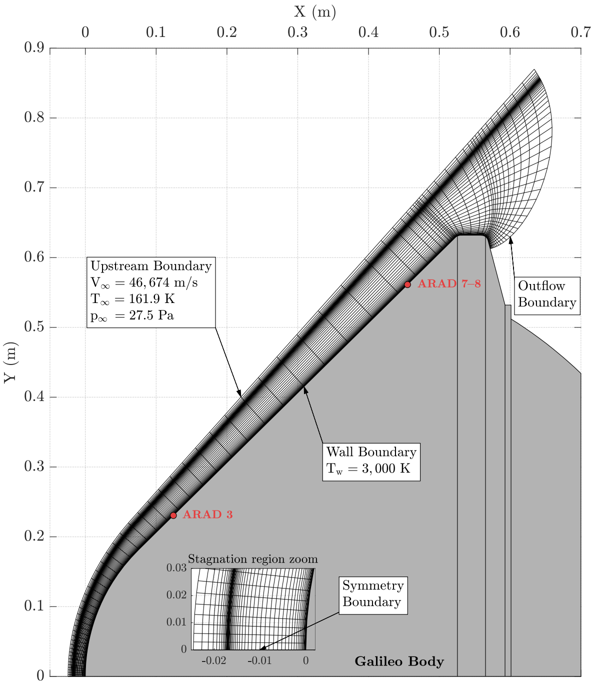

**Figure 6:** Computational mesh and boundary conditions.

## 5.1. General Flowfield Features

Figure 7 compares the stagnation line temperatures and convective heating obtained for the four cases considered. The maximum temperature predicted using the Gupta/Yos transport model is about 28,000 K at the shock for the non-equilibrium case, 6% higher than that obtained under equilibrium conditions. The non-equilibrium region extends for 3–4 mm after the shock, a small thickness that will be critical when discussing $H_2$ radiation. Thermal equilibrium is then attained up to the boundary layer, where the imposed wall temperature induces the large gradients observed. Similar considerations apply to the Wilke 1T and 2T cases. A 5% higher peak temperature is predicted using Wilke's transport model as a result of the lower thermal conductivities, since the shock is thinner and the heat does not diffuse at the rate predicted with the Gupta/

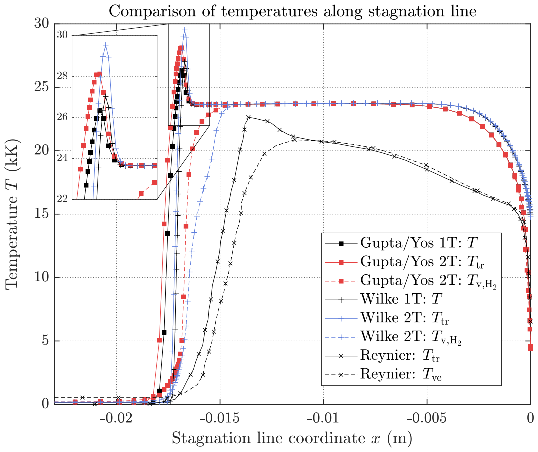

**(a)** Temperatures along stagnation line.

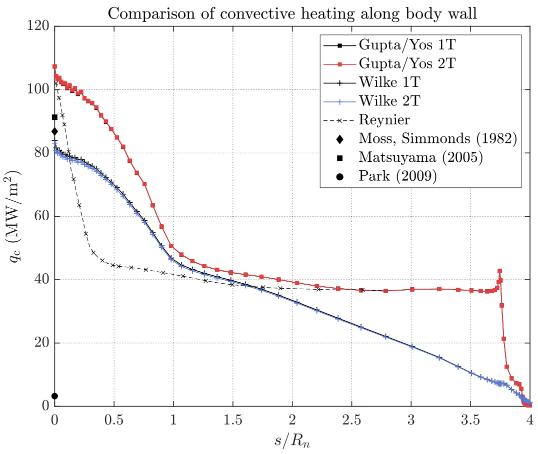

**(b)** Convective heat fluxes along body.

**Figure 7:** Comparison of flowfield properties.

Yos model. The Wilke boundary layer gradients are not well captured due to poor mesh refinement at the wall, despite the $72 \times 90$ mesh used for this case. As mentioned in [1], a first-cell height of 20 nm was required to solve this problem, which proved unfeasible in the present work. Also, the discrepancies observed with Reynier *et al.*'s temperature profiles are a result of different kinetic rates and thermodynamic databases employed.

As a result of the difficulty encountered in Wilke's case, the convective heat fluxes presented in Figure 7b are underpredicted. A good agreement is found between the Gupta/Yos cases and Reynier *et al.*'s prediction in the conical body section, which doesn't translate to the spherical section, where the Gupta/Yos heat fluxes are larger by up to a factor of two. Regardless of the transport model employed, thermal non-equilibrium doesn't appear to have an impact in convective heating. Finally, the local peak near the shoulder is a result of the rapid expansion that reduces the boundary layer thickness and leads to higher temperature gradients, increasing TPS recession in the shoulder corner.

### 5.2. Radiative Heating Sensitivity Studies

Several sensitivity studies on the radiative heating experienced by the Galileo probe are now presented, so that the assumptions used in past predictions can be appraised. Following the discussion on the impact of the transport model and thermal non-equilibrium, the radiative heating is also influenced by virtue of the different number density and temperature fields obtained. Figure 8 illustrates the effects of transport, thermal equilibrium and radiative transfer models on the radiative heating along the body, where the constant coefficient ray-tracing model was used unless stated otherwise.

Clearly, the overpredicted heat fluxes obtained with the Wilke model are consistent with the unrealistically high boundary layer temperatures resulting from insufficient refinement near the wall. However, the larger shock temperatures predicted by this model also contribute to the discrepancy observed between the Wilke and Gupta/Yos formulations. Thus, it is difficult to conclude whether the overprediction is a result of the poor mesh refinement or a manifestation of the inaccuracy of the former model at high temperatures. Moreover, the results obtained with the Wilke transport model show a continuous increase in radiative heating towards the shoulder, as opposed to the slow decline observed with Gupta/Yos. It is interesting to note that this trend conforms with the higher shoulder heat fluxes identified during post-flight data analysis, despite the inaccuracies of the model at high temperatures.

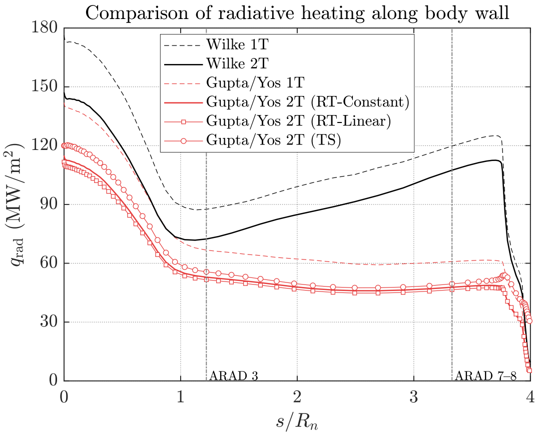

**Figure 8:** Modeling influence on radiative heating.

Regarding non-equilibrium effects, the thermal equilibrium solution predicts 25% higher radiative fluxes compared to the 2T model. This stems from strong $H_2$ emission at the shock, and is caused by considering the translational and vibrational temperatures to be in equilibrium. In reality, vibrational relaxation occurs at a finite rate, and $T_{\mathrm{v},\mathrm{H}_2}$ doesn't reach the $26,000$ K peak predicted by the 1T case. Thus, de-excitation takes place from less energetic vibrational states, resulting in weaker emission.

The radiative transfer model employed also plays an important role in the radiative heating prediction. The results display 3 to 10% higher radiative heat fluxes when the tangent-slab is used over the conventional ray-tracing approach. This difference increases to between 6% and 13% when the comparison is carried over to the more accurate linear interpolation ray-tracing, which differs from the constant coefficient model by 3% throughout the body.

An important outcome of the present work is to understand the effects of He, $He^+$ and $H_2$ systems on the radiative heating, as previous predictions have almost exclusively considered atomic hydrogen only. To this end, the spectral heat fluxes considering all radiative systems are compared in Figure 9 to those using only H systems. The solid lines, representing the cumulative integration along the spectrum, show that the main contribution to the 9.5% difference results from the VUV continuum emission due to $H_2$ radiative recombination. This difference reaches a 1.7% minimum at ARAD 7–8, suggesting the effect of He, $He^+$ and $H_2$ radiation is more important at the SP. The contribution from $H_2$ was observed to originate from the shock location, where temperatures are highest, before dissociation consumes the $H_2$ available in the freestream. Therefore, it highly depends on the shock thickness, which was seen to vary with the transport model used, due to energy diffusion caused by high thermal conductivities. This may lead to an underprediction of radiative emission at the shock if the transport model is unable to predict the high thermal conductivities associated

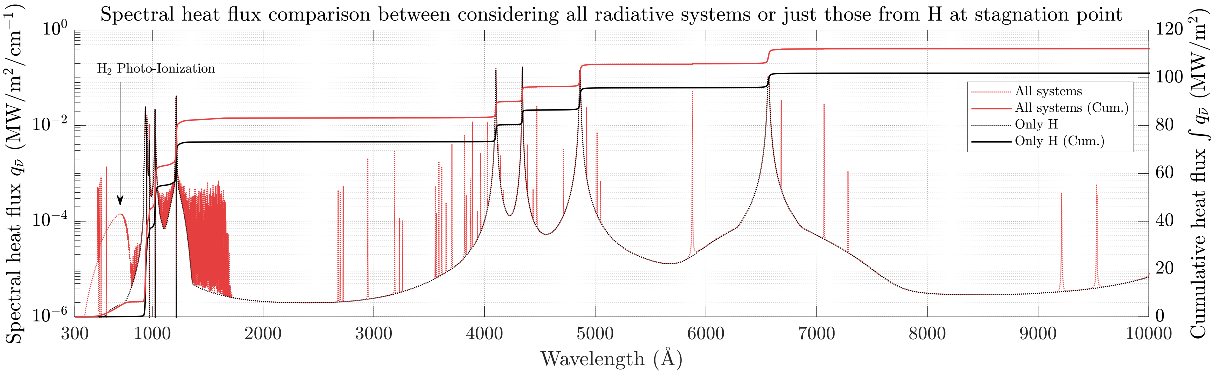

**Figure 9:** Effect of He, $He^+$ and $H_2$ radiative systems on spectral heat flux at the SP using ray-tracing approach on the *Gupta/Yos 2T* solution.

with highly ionized flows.

Up to this point, the effects of precursor heating, ablation products injection and radiation-flowfield coupling have been neglected. These were studied in the present work in an approximate manner, due to a lack of available computational resources. Precursor heating effects result from photo-ionization and photo-dissociation processes occurring before the shock due to radiation emitted upstream from the shock layer. The internal degrees of freedom of $H_2$ are excited, increasing $T_{v,H_2}$. The flowfield changes promoted by these effects were imposed to the *Gupta/Yos 2T* solution based on previous work done on the subject [7]. A 209% increase in radiative heating was observed at the SP, mainly due to the extra molecular band radiation from $H_2$ in the upstream. This suggests that if precursor heating is accounted for, the emission from $H_2$ systems cannot be neglected as was done in the past.

The injection of ablation products in the flowfield was estimated using Park's mole fractions for C, $C^+$, $C_2$ and $C_3$ at the boundary layer [11]. Similarly, the flowfield changes induced by the inclusion of these species were done as a post-processing step to the *Gupta/Yos 2T* solution. The ensuing radiative analysis resulted in the spectral heat fluxes depicted in Figure 10. If these species are injected and reduce the flowfield's temperature to $3,000$ K near the wall, a 74% decrease in radiative heating is observed at the SP. However, the $3,000$ K assumption is conservative, and in the opposite limiting case where ablation products injection is unable to induce a temperature reduction, the additional emission from these species increases the SP heat fluxes by 438%, suggesting that an accurate modeling of ablation products-flowfield energy exchanges is vital to properly estimate its effects on radiative heating.

Finally, the empirical Tauber-Wakefield (TW) correlation was used to estimate the effects of radiation-flowfield coupling. Such formulas, which depend on the local radiative heat flux, are known to underestimate the radiative cooling effect at downstream regions, due to its non-local character. This is indeed observed in Figure 11. The decrease in radiative heating is significant all along the body, but more so in the stagnation region. The results of Moss and Simmonds for the altitudes of 184.5 km (40 s) and 166.6 km (43 s) reveal the same trend obtained with the Wilke model with heat fluxes increasing towards the shoulder. The SP prediction is within the bounds reported by Matsuyama for the altitudes of 184.5 km and 166.60 km, obtained using a tangent-

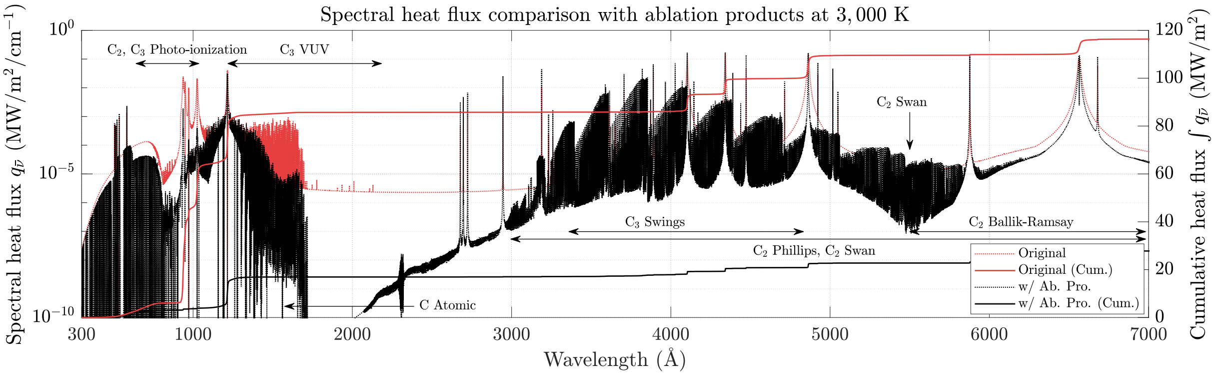

**Figure 10:** Spectral heat fluxes at SP when ablation products are present in the $3,000$ K boundary layer.

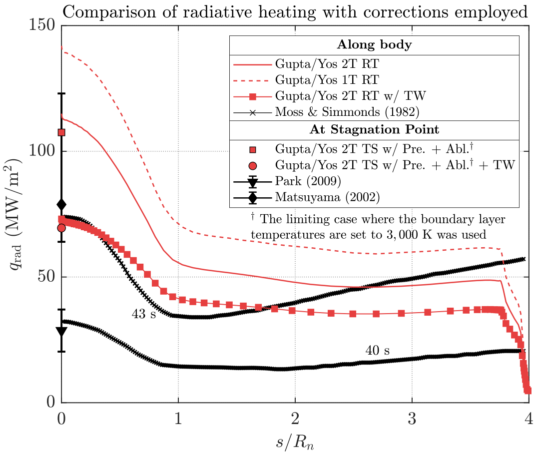

**Figure 11:** Comparison of corrected radiative heating predictions with literature results.

slab approach coupled to an equilibrium flowfield, and only considering H and $H^+$ radiation. Park's prediction, which properly treats ablation products injection, is significantly lower, but again thermochemical equilibrium was assumed. This limits the conclusions that may be drawn from such comparisons. Two additional points were included at the SP in Figure 11. Both show how the combined effect of precursor heating and ablation product absorption almost cancel, provided the conservative case for ablation product temperatures is used.

## 6. Conclusions

Despite the practical nature of this dissertation, a substantial amount of code development was necessary, so as to improve the models applied in the past to Galileo's entry. The transport module in SPARK was re-structured to integrate the modern trend in CCS databases, and the ray-tracing algorithm in SPARK LbL was re-built in OOP Fortran standards.

When applied to Galileo's entry, the Wilke model predicts a narrower shock with higher peak temperatures when compared to Gupta/Yos, leading to a substantial overprediction in radiative heating. $H_2$ radiation was found to play an important role in entry to Jupiter, especially when precursor heating effects are accounted for. Also, thermal nonequilibrium effects must be accurately modeled so as to avoid the vibrational temperature peak prediction under equilibrium conditions. If precursor heating is neglected, inclusion of He, $H^+$ and $H_2$ radiation increases radiative heating by 9.5% at the SP.

Ablation products absorption was shown to potentially counteract the effects of $H_2$ precursor heating. However, the ablation layer temperature must be accurately predicted using a material-response code coupled to the flowfield. Although a 74% decrease in radiative heating is observed in the conservative case, the 438% increase predicted otherwise reveals the uncertainties one may expect to deal with if ablation product-flowfield energy exchanges are not properly modeled. Finally, the analysis conducted on the effects of three-dimensional radiation modeling reveals a maximum 10% difference between the tangent-slab and ray-tracing approaches at the SP.

## Acknowledgements

The author would like to thank Prof. Mário Lino da Silva for all the support and the opportunity to present the results at the 8th International Workshop of Radiation and High-Temperature Gases.

## References

[1] Reynier, P. *et al.*, Progress in Aerospace Sciences **96**, 1–22 (2018).

[2] Milos, F. S. *et al.*, Journal of Spacecraft and Rockets **36(3)**, 298–306 (1999).

[3] Leibowitz, L. P., The Physics of Fluids **16(1)**, 59–68 (1973).

[4] Livingston, F. R. and Y. Poon, P., AIAA Journal **14(9)**, 1335–1337 (1976).

[5] Leibowitz, L. P. and Kuo, T.-J., AIAA Journal **14(9)**, 1324–1329 (1976).

[6] Moss, J. and Simmonds, A., in *3rd Joint Thermophysics, Fluids, Plasma and Heat Transfer Conference*, 874 (1982).

[7] Tiwari, S. N. and Szema, K. Y., in *2nd Thermophysics and Heat Transfer Conference*, vol. 64 (1978).

[8] Matsuyama, S. *et al.*, in *8th AIAA/ASME Joint Thermophysics and Heat Transfer Conference* (2002).

[9] Matsuyama, S. *et al.*, Journal of Thermophysics and Heat Transfer **19(1)**, 28–35 (2005).

[10] Furudate, M. *et al.*, in *44th AIAA Aerospace Sciences Meeting and Exhibit*, vol. 7 (2006).

[11] Park, C., Journal of thermophysics and heat transfer **23(3)**, 417–424 (2009).

[12] Furudate, M., Journal of Thermophysics and Heat Transfer **23(4)**, 651–659 (2009).

[13] Palmer, G. *et al.*, Journal of Spacecraft and Rockets **51(3)**, 801–814 (2014).

[14] Kramida, A. *et al.*, "NIST Atomic Spectra Database (version 5.5.6)", `https://physics.nist.gov/asd` (2018). Accessed: 2018-05-10.

[15] Perrin, M. *et al.*, The Open Plasma Physics Journal **7(1)** (2014).

[16] González, Á., Mathematical Geosciences **42(1)**, 49 (2010).

[17] Johnston, C. O. and Mazaheri, A., Journal of Spacecraft and Rockets **55(4)**, 899–913 (2018).